Dalton Transactions



PAPER View Article Online
View Journal | View Issue



Cite this: Dalton Trans., 2019, 48,

Remarkably improved electrochemical hydrogen storage by multi-walled carbon nanotubes decorated with nanoporous bimetallic Fe-Ag/TiO₂ nanoparticles

Raziyeh Akbarzadeh, ^a Mehrorang Ghaedi, ^b * Syamak Nasiri Kokhdan and Darvoosh Vashaee ^b

Nanoporous bimetallic Fe–Ag nanoparticles (NPs) were synthesized using a facile chemical reduction method and used to decorate the surface of multi-walled carbon nanotubes (MWCNTs) for hydrogen sorption and storage. The effect of TiO_2 nanoparticles on the hydrogen storage properties of Fe–Ag/CNTs was further studied in detail. For this purpose, several nanocomposites of nanoporous bimetallic Fe–Ag/TiO $_2$ nanoparticles with different amounts of bimetallic Fe–Ag NPs were prepared via a hydrothermal method. The hydrogen storage capacity of the as-prepared nanocomposites was studied using electrochemical methods. The Fe–Ag/TiO $_2$ /CNT nanocomposite with 0.04 M bimetallic Fe–Ag NPs showed the highest capacity for hydrogen storage, which was \sim 5x higher than that of pristine MWCNTs. The maximum discharge capacity was 2931 mA h g $^{-1}$, corresponding to a 10.94 wt% hydrogen storage capacity. Furthermore, a 379% increase in discharge capacity was measured after 20 cycles. These results show that Fe–Ag/TiO $_2$ /CNT electrodes display superior cycling stability and high reversible capacity, which is attractive for battery applications.

Received 27th September 2018, Accepted 3rd December 2018 DOI: 10.1039/c8dt03897j

1. Introduction

Hydrogen energy is researched extensively as an alternative to fossil fuels because of critical advantages such as large heat of combustion (287 kJ mol⁻¹), abundant supply, renewability, high efficiency, environmentally compatible by-product (water) and greenhouse gas emissions, *etc.*^{1,2} However, design and development of appropriate hydrogen storage materials with long-lasting stability is a scientific challenge that is crucial for their use in a future hydrogen economy.³⁻⁵ Sodium borohydride (NaBH₄) has emerged as a new and promising hydrogen storage material.⁶⁻⁸

In recent years, great attention has been devoted to the development of new porous materials with high hydrogen sorption ability, such as carbon nanotubes (CNTs), graphene and few-layer graphene. 9-12 CNTs are a good choice for electrochemical hydrogen storage due to their unique physical and chemical properties, such as high specific surface area,

impressive chemical stability, high mechanical ability, low density and high electron-transfer rate. 13,14

There are two hydrogen adsorption pathways in CNTs. First is the physical adsorption of hydrogen molecules, which is favored at a high pressure H₂ atmosphere. Second is electrochemical adsorption of hydrogen, which is applicable in secondary batteries that are beneficial in configuring small-scale energy storage systems.¹⁵ Electrochemical hydrogen storage provides higher capacity at ambient temperature and atmospheric pressure than conventional hydrogen storage technology at low temperature and high pressure.¹⁶

Metals, mainly Ni, Ag, Pd and Pt, or metal oxides, such as ${\rm TiO_2}$ nanocatalysts, decorated onto CNTs lead to an increase in hydrogen storage capacity through a very interesting mechanism called spillover. Metal or metal oxide nanoparticles spill hydrogen over the carbon nanotubes and when their highest content is exposed to hydrogen during the adsorption process the spillover mechanism is achieved. 19,21

Moreover, bimetallic catalyst nanostructures are a good choice for achieving selectivity, stability and superior specific activity in various applications, such as catalysis, ^{22,23} chemical/gas sensors, ²⁴ fuel cells, ^{25,26} hydrogen generation ²⁷ and hydrogen storage, ^{28,29} and are more favorable in sustainable energy technology than their monometallic counterparts. The

^aChemistry Department, Yasouj University, Yasouj 75918-74831, Iran. E-mail: m_ghaedi@mail.yc.ac.ir, m_ghaedi@yahoo.com; Fax: +98 741 2223048; Tel: +98 741 2223048

^bElectrical & Computer Engineering Department, North Carolina State University, Raleigh, NC 27606, USA

Dalton Transactions Paper

addition of the second metal may cause considerable changes in catalytic properties, activity and selectivity.²³

Palladium and platinum, and their bimetallic systems, are a class of interesting materials for storing hydrogen due to their fast adsorption/desorption rates, but their application for hydrogen storage is restricted because of their high cost. ^{17,29–31}

The conspicuous physicochemical catalytic properties, strong structural characteristics and relatively low cost of silver make it a noteworthy material for hydrogen storage. Silver can combine with some other metals, such as iron, to form bimetallic systems. The effect of iron on improving the effective storage capacity of such hydrogen storage alloys has been investigated. In particular, bimetallic Fe–Ag particles exhibited higher hydrogen storage compared to monometallic Fe or Ag particles. This increase in storage capacity is attributed to the strong metal–metal interaction which enhances the hydrogen spillover effect by adjustment of the electronic structure of Ag using Fe. The size and surface site distribution of the particles has a significant influence on the electrochemical response of hydrogen in hydrogen storage materials. ^{29,36,37}

Fast hydrogen diffusion in nanostructured materials significantly improves the kinetics of hydrogen adsorption and desorption.38-40 Therefore, CNTs decorated with bimetallic materials are expected to have the ability of electrochemical hydrogen storage. 29,31 Additionally, metal oxides are attractive, low toxicity and economical energy storage materials for electrochemical capacitor applications.¹⁹ Among the metal oxides, TiO2 with anatase41 and rutile42 phases has attracted much interest and is a promising material for energy storage because of its excellent charge storage capability, high redox activity, low cost and superior electrochemical properties. 43,44 To date, various composites have been developed based on TiO₂ and conductive components such as carbon nanotubes (CNTs), graphene and carbon black. 45-47 Research results have demonstrated that TiO2 nanocatalyst-coated CNTs have better electrochemical storage performance, which enhances their hydrogen storage capacity, than pure CNTs. 45,48,49

Inspired by these findings, we have studied low cost but effective materials with a high capacity for hydrogen storage. In this work, a Fe-Ag/CNT nanocomposite with high hydrogen storage capacity was prepared by coating nanoporous bimetallic Fe-Ag nanoparticles, synthesized by a simple chemical reduction method, onto the surface of oxidized MWCNTs. Moreover, nanoporous bimetallic Fe-Ag/TiO2 nanoparticles with different amounts of Fe-Ag were synthesized using a facile hydrothermal method, and subsequently the effect of TiO₂ nanoparticles on improving the hydrogen storage capacity of Fe-Ag/CNTs nanocomposites was optimized. The absence of any report on the application of nanoporous bimetallic Fe-Ag/TiO₂ nanoparticles decorated onto the surface of CNTs for hydrogen storage encouraged our group to focus on this aspect. The key finding of the present study is the best composition of bimetallic Fe-Ag/TiO₂ nanoparticles that leads to a significant improvement in their hydrogen storage efficiency. Our studies have shown that nanoporous bimetallic Fe-Ag/

 ${
m TiO_2}$ nanoparticles decorated onto the surface of MWCNTs with a composition of 0.04 M Fe–Ag nanoparticles significantly enhance hydrogen storage capacity.

2. Experimental

The chemicals used in this investigation were iron($\rm III$) nitrate nonahydrate (Fe(NO₃)₃·9H₂O), silver nitrate (AgNO₃), trisodium citrate, titanium isopropoxide (TTIP) and multi-walled carbon nanotubes (MWCNTs, outer diameter 10–20 nm, length 20 μ m) purchased from Sigma-Aldrich. Polyvidone 25, sodium borohydride (NaBH₄) and acetic acid were obtained from Merck. Absolute ethanol and deionized water were used during the preparation of powders. All chemicals were used without further purification.

2.1. Materials characterization

The powder X-ray diffraction (XRD) patterns of the products were determined using a Phillips X'Pert PRO equipped with a Cu K α source having a scanning range of 0–80° Bragg angle. The morphological characterization was obtained using a Phillips XL-30FESEM field emission scanning electron microscope (FESEM) equipped with an energy dispersive X-ray analyzer (EDS). Elemental distribution of the samples was revealed using a HAADF-STEM-FEI Titan 80–300 high-angle annular dark-field scanning transmission electron microscope (HAADF-STEM) equipped with EDS. EDS spectroscopy and elemental mapping were used for compositional analysis and to investigate the homogeneity of the elemental distribution. Raman spectra were measured with a Takram P50C0R10 Teksan dispersive Raman spectrometer equipped with a 532 nm Nd:YLF laser as the excitation source.

2.2. Preparation of nanoporous bimetallic Fe-Ag nanoparticles and Fe-Ag/CNT nanocomposites

The nanoporous bimetallic Fe–Ag NPs were prepared as follows: 5 ml 0.02 M Fe(NO $_3$) $_3\cdot$ 9H $_2$ O, 5 ml 0.034 M tri-sodium citrate and 10 ml 0.5 g polyvidone 25 (which all dissolved in deionized water) were diluted by 20 ml of deionized water. The mixed solution was stirred for 15 min at ambient temperature under an argon atmosphere and subsequently 0.3 g sodium borohydride in 20 ml deionized water was added dropwise. After 1 h stirring, 5 ml 0.01 M AgNO $_3$ and 10 ml sodium borohydride solution (0.2 g NaBH $_4$) were added dropwise into the solution. After 2 h of stirring, the colloidal solution obtained was centrifuged at 12 000 rpm for 10 min and washed several times with deionized water and absolute ethanol and the pH was adjusted to 7. The final product was dried in a vacuum oven overnight at 50 °C for 24 h.

The Fe-Ag/CNT nanocomposite was prepared by reduction of $Fe(NO_3)_3 \cdot 9H_2O$ and $AgNO_3$ precursors and loaded onto an oxidized MWCNT suspension. A chemical oxidation method was used to implant various oxygen-containing species onto the MWCNTs according to the literature. First, 0.04 g oxidized MWCNTs were mixed with 5 ml 0.02 M $Fe(NO_3)_3 \cdot 9H_2O$

Paper

solution and stirred under air atmosphere for 2 h. Then the process described above was performed, and after adding additional sodium borohydride solution, the mixture was stirred for 24 h.

2.3. Preparation of nanoporous bimetallic Fe-Ag/TiO₂ nanoparticles and Fe-Ag/TiO₂/CNT nanocomposites

In a typical procedure, 2 ml of the above-described nanoporous, bimetallic Fe–Ag NPs, with concentrations of 0.01, 0.04 and 0.1 M, were dispersed in 30 ml absolute ethanol for 15 min and then 1 ml acetic acid was added and sonicated for another 30 min. In the next step, 0.2 ml TTIP was added dropwise into the mixture and, after 1 h stirring at room temperature, the suspension was transferred into a Teflon-lined autoclave, which was sealed and heated at 150 °C for 12 h. After cooling to room temperature, this solution was centrifuged at 7000 rpm for 10 min. The precipitate was washed with deionized water and absolute ethanol once more. Finally, the bimetallic Fe–Ag/TiO $_2$ NPs were dried in air at 80 °C for 12 h and their products labeled as (0.01)Fe–Ag/TiO $_2$, (0.04)Fe–Ag/TiO $_2$ and (0.1)Fe–Ag/TiO $_2$.

The typical process utilized for supporting the oxidized carbon nanotubes with nanoparticles was as follows. To prepare a colloidal suspension of CNTs, 2 mg oxidized MWCNTs were dispersed in 20 ml deionized water under sonication for 30 min. Then, 2 mg of as-prepared bimetallic Fe–Ag/TiO $_2$ nanoparticles were added to the scattered solution and dispersed for 24 h. Finally, the products were collected by centrifugation, washed with deionized water and absolute ethanol three times and dried at 80 °C for 12 h.

2.4. Preparation of working electrodes

Copper foam with nano-sized pores was washed with acetone and deionized water and subsequently dried under vacuum conditions at 70 °C for 2 h. The as-prepared nanocomposites were ultrasonically dispersed in 1 ml of 1:1 v/v deionized water: 2-propanol and a few drops of Nafion 0.5 wt% mixture for 30 min. Then, pure copper foam with a surface area of 1×1 cm² was coated with a thin layer of a sonicated solution of the sample at 100 °C.

2.5. Electrochemical measurements

A Sama 500 potentiostat electrochemical workstation (Isfahan, Iran) equipped with the three-electrode system was employed for electrochemical studies at ambient temperature and pressure in 6.0 M KOH aqueous solution. The platinum plate and Ag/AgCl were used as the counter and reference electrodes, respectively. For charging/discharging experiments, the prepared working electrodes were fully charged at a current density of 11 000 mA $\rm g^{-1}$ for 30 min followed by 5 min rest and then discharged at 4000 mA $\rm g^{-1}$. The discharge cell potential cutoff was set to 0.34 V.

Cyclic voltammetry (CV) measurement of the working electrodes was done in a potential range of -1.2 to 0 V νs . Ag/AgCl electrode at a scan rate of 100 mV s⁻¹.

3. Results and discussion

The phase and purity of the samples were confirmed by powder X-ray diffraction (XRD). Fig. 1a shows the XRD pattern of nanoporous bimetallic Fe-Ag NPs which is composed of a few sharp diffraction peaks appearing at 2θ values of ca. 38.2°, 44.6°, 64.7° and 77.7°, corresponding to the (111), (200), (220) and (311) crystal planes of the face-centered-cubic (fcc) silver (JCPDS no. 87-0717), respectively. The two distinct peaks at 44.6° and 64.7° are readily assigned to the characteristic (110) and (200) diffractions of fcc iron (JCPDS no. 01-1262), but the Ag peaks prevailed over the Fe peaks. The non-observance of iron peaks in the bimetallic sample, which has about 57% iron, is perhaps due to Fe particles that are surrounded by Ag atoms, and this is further confirmed by FESEM and STEM images. It is clear that there was no significant peak shift, representing Fe and Ag phase separation, as well as the nonexistence of Fe-Ag alloy.

Fig. 1 also depicts XRD patterns for the bimetallic Fe-Ag/ TiO₂ nanoparticles synthesized with different concentrations of bimetallic Fe-Ag NPs, which display typical characteristic peaks for anatase TiO2 (JCPDS no. 04-0477). The diffraction peaks of the (004) crystal plane of anatase TiO₂ and the (111) plane of Ag overlapped with each other. The XRD profile of (0.01)Fe-Ag/TiO₂, as can be seen, has no peaks related to Fe and Ag (Fig. 1b), which may be due to the low concentration and high dispersion of metal species on the TiO₂ surface.⁵¹ Increasing the concentration of Fe-Ag NPs leads to the appearance of characteristic peaks assigned to the presence of metals, as observed in the XRD patterns of (0.04)Fe-Ag/TiO₂ (Fig. 1c) and (0.1)Fe-Ag/TiO₂ (Fig. 1d). The absence of additional peaks belonging to the impurity phase in all the XRD patterns indicates the high purity of the samples obtained.

As calculated from the full-width at half-maximum (FWHM) of the (101) reflection peaks, the average crystallite sizes of bimetallic (0.01)Fe-Ag/TiO₂, (0.04)Fe-Ag/TiO₂ and (0.1)Fe-Ag/TiO₂ samples are 14.2, 9.3 and 10.4 nm, respectively, according

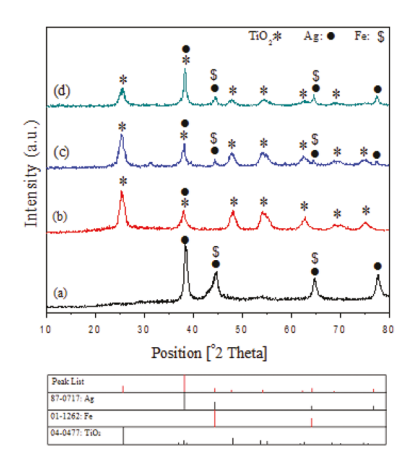


Fig. 1 The XRD patterns of bimetallic (a) Fe-Ag (b) (0.01)Fe-Ag/TiO₂ (c) (0.04)Fe-Ag/TiO₂ and (d) (0.1)Fe-Ag/TiO₂ nanoparticles.

Dalton Transactions Paper

to Scherrer's formula ($D = 0.89\lambda/\beta\cos\theta$), where D, λ , θ and β are, respectively, the averaged dimension of crystallites, the wavelength of Cu K α_1 radiation (0.1541 nm), the Bragg angle of the peak and the FWHM peak in radians. It can be seen clearly that the smallest average particle size is related to Fe–Ag/TiO₂ nanoparticles with 0.04 M of bimetallic Fe–Ag NPs. This reduced particle size causes an increased surface area and significantly enhances the ability to adsorb hydrogen.

The XRD patterns of bimetallic Fe-Ag and Fe-Ag/TiO₂ nanoparticles decorated onto the surface of MWCNTs are given in Fig. 2A. The peak at around 2θ = 26.3°, belonging to the (002) plane corresponds to the MWCNTs, and overlaps with the

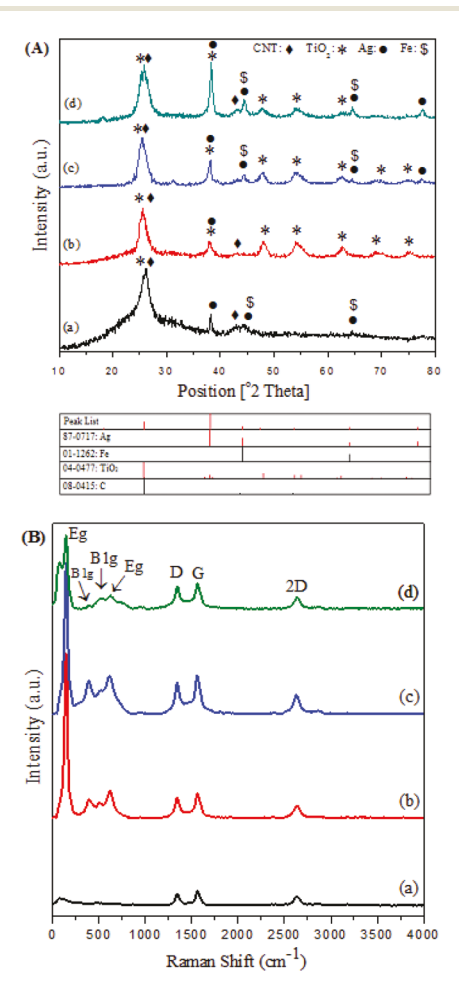


Fig. 2 (A) The XRD patterns and (B) Raman spectra of (a) Fe-Ag/CNT (b) (0.01)Fe-Ag/TiO₂/CNT (c) (0.04)Fe-Ag/TiO₂/CNT and (d) (0.1)Fe-Ag/TiO₂/CNT nanocomposites.

intense peak of anatase TiO₂ (101) in Fe-Ag/TiO₂ NPs decorated on MWCNT samples. As can be seen in Fig. 2A, the XRD patterns of Fe-Ag/CNT and Fe-Ag/TiO₂/CNT nanocomposites are almost identical to those of bimetallic Fe-Ag and Fe-Ag/TiO₂ (Fig. 1), respectively, which confirms the absence of a significant change in the structure following loading on MWCNTs. No apparent impurity phase is observed in any of the XRD patterns.

The structure and crystallinity of Fe–Ag/CNT, (0.01)Fe–Ag/TiO₂/CNT, (0.04)Fe–Ag/TiO₂/CNT and (0.1)Fe–Ag/TiO₂/CNT nanocomposites was further analyzed using Raman spectroscopy (Fig. 2B) and a summary of the results is shown in Table 1. The typical Raman active modes of anatase TiO₂ ($D_{4\rm h}$ point group) are composed of four peaks at the low-frequency region around 147 (Eg), 395 (B_{1g}), 514 (B_{1g}) and 636 cm⁻¹ (Eg). It can be deduced that all the constructed samples are in the anatase phase without any evidence for the presence of the rutile phase, which is in good agreement with the XRD studies.

In general, the D (1350 cm⁻¹) and G (1585 cm⁻¹) bands characteristic of graphite-based carbons⁷ were observed in all experiments. The D band is mainly due to the presence of sp³ defect-induced disordering in carbon systems and the G band is related to the vibration of the sp²-bonded carbon atoms of graphite. 52 The peak at 2633 cm⁻¹ corresponds to the second harmonic of the D (G' or 2D) peak. The I_D/I_G intensity ratio of the peaks is used as a rough measure of sample quality.⁵³ The slight increase in I_D/I_G ratio implied that more defects are formed due to the presence of TiO2 in Fe-Ag/TiO2/CNT nanocomposites. Meanwhile, the high I_D/I_G ratio is suggestive of a defect in the carbon structure which can facilitate diffusion of H⁺ ions through the disordered region. On the other hand, the defects created facilitate the spillover of hydrogen from nanoporous bimetallic Fe-Ag/TiO2 nanoparticles to carbon nanotubes. The increase in the quality of the bimetallic (0.04)Fe-Ag/TiO2 nanoparticles decorated onto MWCNTs, in comparison with the two other samples, indicates that the structure appearing in the presence of 0.04 M bimetallic Fe-Ag NPs leads to the destruction of MWCNT structures. Therefore, preparation of a well-suited Fe-Ag/TiO2/CNT nanocomposite with an appropriate amount of nanoporous bimetallic Fe-Ag NPs is crucial.

Fig. 3A and B represent typical FESEM images of the nanoporous bimetallic Fe-Ag NPs which approximately confirm the nanoporous and homogeneous string structure consisting of irregular pores several nanometers in diameter. These results can be explained based on the large-scale Fe nanoparticles being surrounded by small Ag nanoparticles that create a

Table 1 List of the vibrational frequencies (cm⁻¹) derived from the Raman spectra

Samples	TiO ₂ peak position (cm ⁻¹)	D band (cm ⁻¹)	G band (cm ⁻¹)	$I_{ m D}/I_{ m G}$
Fe-Ag/CNT	—	1344	1561	0.75
(0.01)Fe-Ag/TiO ₂ /CNT	147, 391, 507, 620	1344	1561	0.81
(0.04)Fe-Ag/TiO ₂ /CNT	147, 391, 501, 620	1342	1557	0.88
(0.1)Fe-Ag/TiO ₂ /CNT	147, 389, 519, 626	1343	1561	0.85

Dalton Transactions Paper

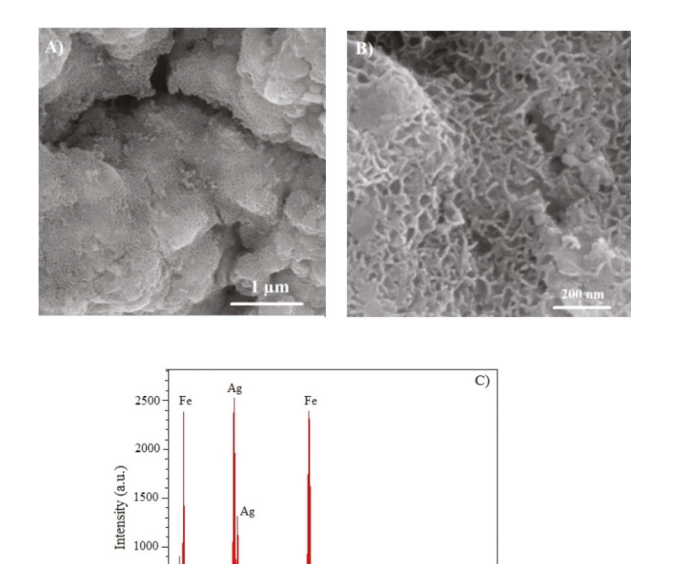


Fig. 3 (A) and (B) FESEM images and (C) EDS line profile of nanoporous bimetallic Fe-Ag nanoparticles.

500

nanoporous morphology that provides the large surface area required for hydrogen adsorption. The EDS line profile (Fig. 3C) suggests that the bimetallic Fe-Ag structure consists of two parts, one rich in Fe (57%) and one rich in Ag (43%).

High-angle annular dark-field scanning transmission electron microscopy (HAADF-STEM) was successfully applied to further characterize the morphology and elemental distribution of nanoporous bimetallic Fe-Ag nanoparticles. Fig. 4

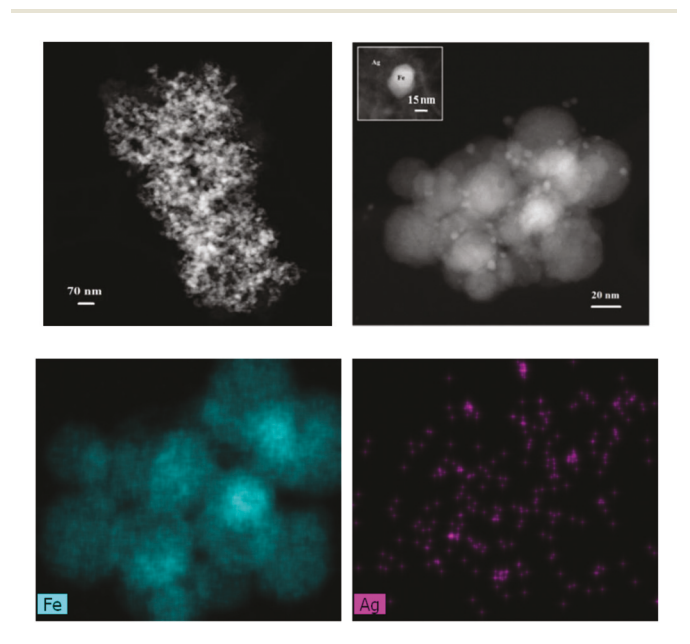


Fig. 4 STEM and elemental mapping images of nanoporous bimetallic Fe-Ag nanoparticles.

clearly shows that the Fe nanoparticles with an average particle size of 25-35 nm are surrounded by a large number of very small Ag atoms that create a porous structure. The elemental mapping images revealed the segregation of the Fe and the Ag particles without alloying phenomena.

The FESEM images and particle size distribution, according to digimizer software, of bimetallic Fe-Ag/TiO2 nanoparticles synthesized with different concentrations of bimetallic Fe-Ag NPs are shown in Fig. 5. The bimetallic (0.01)Fe-Ag/TiO₂ sample is comprised of aggregated particles with low homogeneity. Increasing the content of the bimetallic Fe-Ag NPs, from 0.01 to 0.04 and 0.1, lead to the formation of particles of uniform size and morphology. The bimetallic (0.04)Fe-Ag/TiO₂ sample is composed of separate and free aggregate nanoparticles (Fig. 5C) with an average particle size in the range 8-10 nm, in comparison with 14-16 nm for (0.01)Fe-Ag/TiO₂ and 8-12 nm for (0.1)Fe-Ag/TiO2, which is consistent with the results of XRD. The porous structure and reduction in particle size leads to an increase in surface area which is desirable for hydrogen sorption and storage. The EDS line profile, as shown in Fig. 5G, strongly supports that the elements present are Fe, Ag, Ti and O.

The surface morphology of the nanoporous bimetallic (0.04)Fe-Ag/TiO₂ nanoparticles decorated on the surface of MWCNTs was examined by FESEM as shown in Fig. 6A, which strongly shows the uniform formation of nanoparticles and their high dispersion on the external wall of the MWCNTs with a spherical morphology. The average particle size is 8.0-10 nm from measuring more than 100 nanoparticles. The high dispersion of bimetallic Fe-Ag/TiO₂ nanoparticles on the MWCNT surface is one of the most important reasons for the improvement in hydrogen storage capacity. As shown in Fig. 6B, the EDS line profile confirms the existence of Fe, Ag, Ti, O and C elements. In addition, the distribution of nanoparticles on the surface of MWCNTs was analyzed by elemental mapping (Fig. 7). The results clearly reveal deposition of Fe, Ag and TiO₂ nanoparticles on the surface of MWCNTs.

A schematic of the synthetic process for the preparation of Fe-Ag/TiO2 nanoparticles decorated on the surface of MWCNTs is shown in Fig. 8.

To explore the electrochemical hydrogen storage performance of the as-prepared nanocomposites, a three-electrode cell in a 6 M KOH solution was assembled (see Experimental section for details) and the charge and discharge curves were recorded as shown in Fig. 9A and B. The amount of hydrogen stored, calculated from the measurement of released hydrogen from various samples, and the discharge capacities are listed in Table 2. The discharge capacity of copper foam before coating is less than 1 mA h g⁻¹ (Fig. 9C) which proves the low and negligible contribution of copper foam to the discharge capacity of the samples.

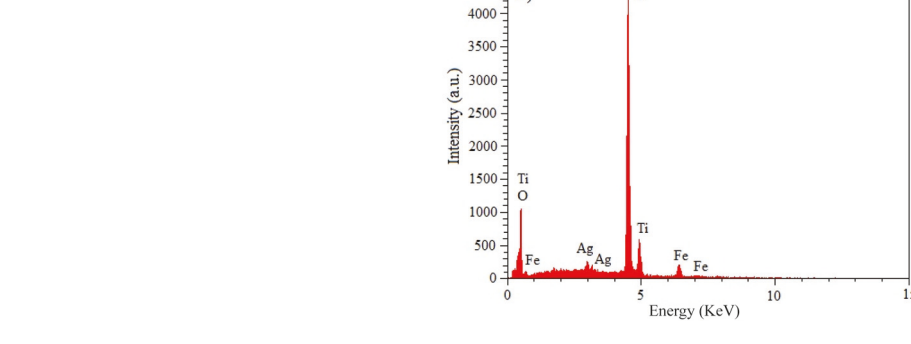
As shown in Fig. 9B and Table 2, the discharge capacity of the Fe-Ag/CNT electrode is 1103 mA h g⁻¹ which is higher than that of the Ag/CNT electrode (845 mA h g⁻¹). This is probably related to strong electronic interactions between Fe and Ag, which significantly boosts the hydrogen electrosorption properties of Ag.

Dalton Transactions

10 12

Particle size (nm)

14 16



2

8 10 12 14 16 18 20 22

Particle size (nm)

Fig. 5 FESEM images and particle size distributions of bimetallic nanoparticles: (A) and (D) $(0.01)\text{Fe}-\text{Ag/TiO}_2$; (B) and (E) $(0.04)\text{Fe}-\text{Ag/TiO}_2$; (C) and (F) $(0.1)\text{Fe}-\text{Ag/TiO}_2$. (G) EDS analysis of $(0.04)\text{Fe}-\text{Ag/TiO}_2$ sample shown in (B).

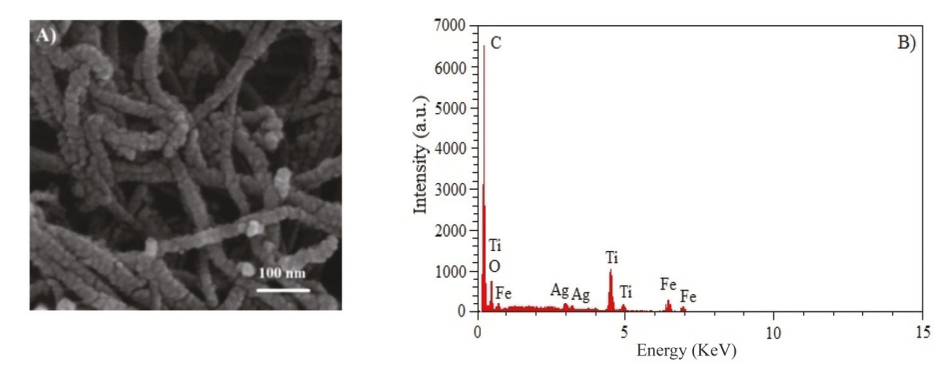


Fig. 6 (A) FESEM and (B) EDS line profiles of nanoporous bimetallic (0.04)Fe-Ag/TiO₂ nanoparticles decorated on the surface of MWCNTs.

It is clearly seen in Fig. 9B that the presence of TiO₂ in the Fe-Ag/CNT nanocomposite has a significant influence on the improvement of the spillover phenomenon and discharge

capacity of the samples. TiO₂ nanoparticles have outstanding redox ability and serve as a catalyst, which can enhance the reduction of H⁺ and the oxidation of H atoms.⁵⁴ The discharge

4

6

8 10 12 14 16 18 20

Particle size (nm)

Paper Dalton Transactions

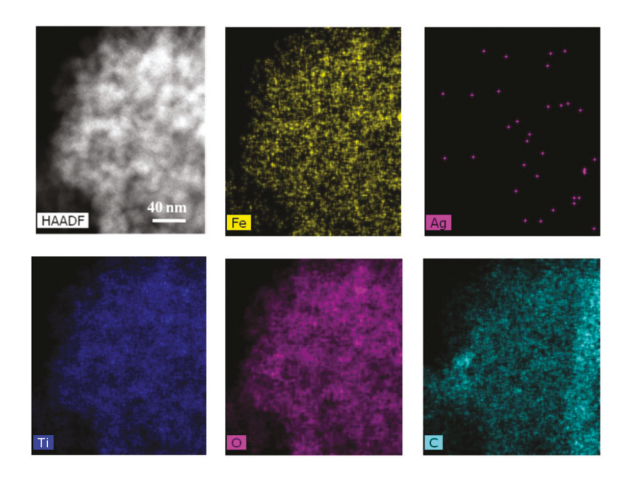


Fig. 7 Elemental mapping images of nanoporous bimetallic (0.04)Fe-Ag/TiO₂ nanoparticles decorated on the surface of MWCNTs.

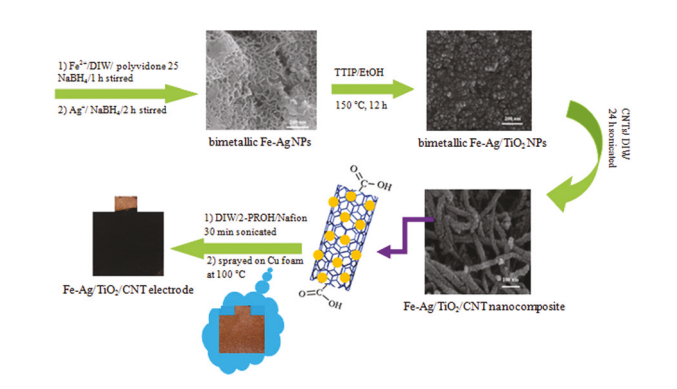


Fig. 8 Schematic diagram illustrating synthesis of the Fe-Ag/TiO₂/CNT electrode

capacity of the (0.1)Fe-Ag/TiO₂/CNT electrode is higher than that of (0.01)Fe-Ag/TiO₂/CNT but lower than that of (0.04)Fe-Ag/TiO₂/CNT. The maximum discharge capacity of 2931 mA h g⁻¹ was obtained for the (0.04)Fe-Ag/TiO₂/CNT electrode, which is higher than that of the other two electrodes. It was noteworthy that higher Fe-Ag content can wall up the channels of the MWCNTs and reduce the effective positions for adsorption of H⁺ ions on MWCNTs. This leads to a lower discharge capacity, by preventing hydrogen entrance into the tube.

It can be deduced that the hydrogen storage capacity of the (0.04)Fe-Ag/TiO2/CNT electrode was 10.94 wt%, which is an improvement of nearly 499% for hydrogen storage capacity in comparison with pristine MWCNTs. The enhancement of about 5 times is due to the interfacial diffusion of hydrogen from the Fe-Ag/TiO2 nanoparticles to the carbon nanotube surface. Furthermore, as shown in Fig. 9B, the discharging plateau tends to become more stable for the Fe-Ag/CNT electrode in the presence of TiO2. For MWCNT and Fe-Ag/CNT, the discharging voltage plateau was observed at about 0.46 V and 0.48 V, respectively, while for the Fe-Ag/TiO2/CNT electrodes the discharging voltage plateau was seen at 0.58 V.

As a result, TiO₂ nanoparticles can significantly improve the adsorption of hydrogen atoms on the surface of Fe-Ag/ CNT nanocomposites. The results reveal that by controlling the content of nanoporous bimetallic Fe-Ag NPs, Fe-Ag/TiO₂/ CNT nanocomposites reach their highest discharge capacity guickly. The Fe-Ag/TiO₂/CNT nanocomposite with the optimum composition of 0.04 M bimetallic Fe-Ag NPs significantly enhances the hydrogen storage capacity of MWCNTs, from 2.19 wt% to 10.94 wt%. Fig. 9D and E show the cycle life and stability for electrochemical hydrogen storage of the (0.04) Fe-Ag/TiO2/CNT electrode. A high and stable discharge capacity of 11 108 mA h g⁻¹ is achieved after 20 cycles which is quite interesting with regard to battery applications compared with other materials. 17,29,48,55 This finding shows excellent cycle stability and a high degree of electrochemical reversibility in the repetitive charge/discharge tests.

Cyclic voltammetry (CV) curves were recorded to investigate the electrochemical hydrogen adsorption/desorption behavior of the Fe-Ag/CNT and (0.04)Fe-Ag/TiO2/CNT electrodes, as shown in Fig. 10. In the cathodic direction, one broad hydrogen reduction peak is clearly observed at -0.95 V, which generally corresponds to electrochemical hydrogen adsorption on the surface of the Fe-Ag/TiO2/CNT electrode, while for the Fe-Ag/CNT sample the peak is around -1.0 V. 9,48,56

During the reverse scan, the anodic current peak appears around -0.5 V and -0.44 V for the Fe-Ag/TiO2/CNT and Fe-Ag/ CNT electrodes, respectively, which is related to electrochemical desorption of the hydrogen adsorbed onto the surface of the electrode material.^{9,57} It can be deduced from the curves that introducing TiO2 into the Fe-Ag/CNT nanocomposite leads to movement of the cathodic reduction and anodic oxidation peaks in the positive and negative potential directions, respectively.

These results indicate easier oxidation of H atoms and reduction of H⁺, which can be attributed to the preferential redox ability of TiO2 nanoparticles. Moreover, the negative shift in the oxidation peaks suggests strong chemisorption of hydrogen (atomic hydrogen bonded to CNTs).⁵⁸

Furthermore, the considerable increase in the current density of the hydrogen adsorption/desorption peaks implies that the presence of TiO2 NPs improves the electrochemical hydrogen storage capacity of Fe-Ag/CNT.

Based on the above discussion, the mechanism for the electrochemical hydrogen storage process of the Fe-Ag/TiO₂/ CNT nanocomposite electrodes can be explained as follows.48,59

$$\label{eq:Fe-Ag/TiO2} \begin{split} \text{Fe-Ag/TiO}_2 + x \text{H}_2 \text{O} + x \text{e}^- &\rightleftharpoons \text{Fe-Ag/TiO}_2 \cdot x \text{H}_{\text{ads}} + x \text{OH}^- \end{split} \tag{1}$$

$$Fe-Ag/TiO_2 \cdot xH_{ads} + CNT \rightleftharpoons CNT \cdot xH_{ads} + Fe-Ag/TiO_2$$
 (2)

Bimetallic Fe-Ag nanoparticles can act as redox sites for hydrogen storage which enhances the spillover effect and thereby increases electrochemical hydrogen adsorption on the surface of MWCNTs. Moreover, the high redox activity of TiO2 NPs is advantageous for the decomposition of water molecules

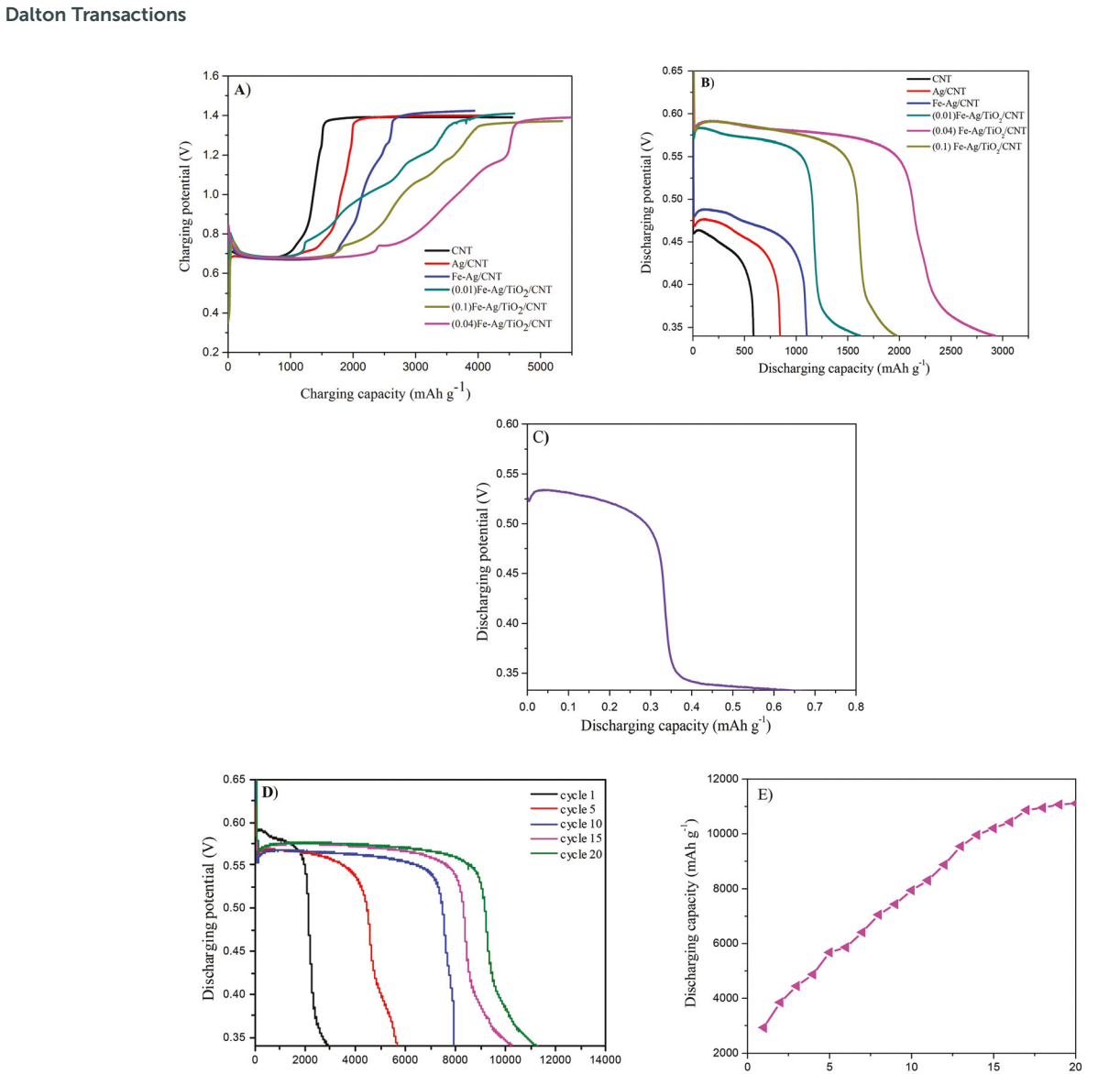
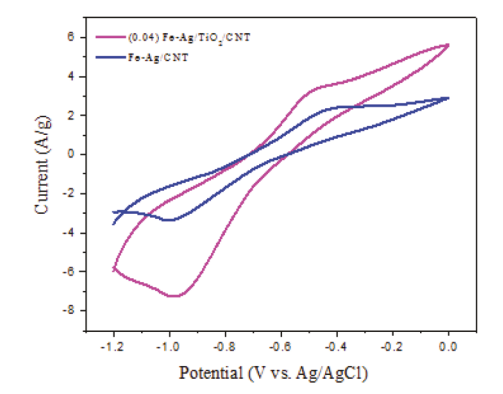


Fig. 9 (A, B) Discharge curves of pristine CNTs, Ag/CNT, Fe-Ag/CNT, (0.01)Fe-Ag/TiO₂/CNT, (0.04)Fe-Ag/TiO₂/CNT and (0.1)Fe-Ag/TiO₂/CNT electrodes; (C) discharge capacity curve of copper foam in the absence of nanocomposites; (D) and (E) cycling performance of (0.04)Fe-Ag/TiO₂/CNT electrode.

 $\textbf{Table 2} \ \ \, \textbf{The discharge and } \ \ \, \textbf{H}_2 \ \, \textbf{storage capacities of the different nanocomposites}$

Discharging capacity (mAh g-1)

Sample	Discharge capacity mA h g ⁻¹	H ₂ storage wt%	
CNT	587	2.19	
Ag/CNT	845	3.15	
Fe-Ag/CNT	1103	4.12	
(0.01)Fe-Ag/TiO ₂ /CNT	1621	6.05	
(0.04)Fe-Ag/TiO ₂ /CNT	2931	10.94	
(0.1)Fe-Ag/TiO ₂ /CNT	1976	7.37	



Cycle number (n)

Fig. 10 Cyclic voltammetry curves of the Fe–Ag/CNT and (0.04)Fe–Ag/TiO $_2$ /CNT electrodes.

Table 3 Hydrogen storage capacity of different reported materials

S. no	Materials used	Hydrogen storage method	H ₂ storage wt%	Ref.
1	Fe-Doped MWCNTs	Electrochemical	1.90	53
2	Pd-Decorated CNTs	Moderate H ₂ pressure	4.50	61
3	Ni-Supported MWCNTs	Electrochemical	6.07	13
4	Ni coated MWCNTs	Moderate H ₂ pressure	1.27	21
5	Co coated MWCNTs	Electrochemical	2.62	56
6	MWCNTs coated Pd-Ni	Moderate H ₂ pressure	2.30	62
7	MWCNTs decorated Pt-Pd	Moderate H ₂ pressure	2.00	17
8	MWCNTs	Electrochemical	1.79	63
9	TiO ₂ -decorated CNTs	Electrochemical	2.02	48
10	Fe-Ag/TiO ₂ /CNT	Electrochemical	10.94	This pape

and the reduction of H^{\dagger} in the charging process and oxidation of H atoms in the discharging process. The presence of TiO_2 on the surface of the Fe–Ag/CNT nanocomposite enhances the surface area for hydrogen adsorption. Thus, the faster electron transfer and larger surface area provide more active sites for adsorption of hydrogen and supply greater electrochemical hydrogen storage capacity.⁵⁴

Comparison of the hydrogen storage capacity of the (0.04) Fe–Ag/TiO₂/CNT nanocomposite in relation to current research with other reported hydrogen storage materials is reported in Table 3. This strongly supports the application of Fe–Ag/TiO₂/CNT nanocomposite under electrochemical processes for hydrogen storage, as it has high hydrogen storage capacity and can deliver performance comparable with other recent hydrogen storage materials. As previously mentioned, electrochemical hydrogen storage is a highly valuable method that provides more capacity than common hydrogen storage technology at low temperature and high pressure.⁶⁰

4. Conclusions

In summary, a novel nanocomposite structure with high hydrogen storage capacity was prepared based on the deposition of nanoporous bimetallic Fe-Ag nanoparticles on the surface of oxidized MWCNTs. TiO2 nanoparticles with high redox ability were used as supplementary adsorbents so that the amount of total adsorbed hydrogen was enhanced significantly. The presence of TiO2 on the surface of the Fe-Ag/CNT nanocomposite increased the surface area and stimulated the Fe-Ag/CNT to reach a large discharge capacity and significantly improved the electrochemical hydrogen storage. Moreover, the capacity for hydrogen sorption and storage depended strongly on the content of bimetallic Fe-Ag nanoparticles. It was found that the Fe-Ag/TiO2/CNT nanocomposite consisting of 0.04 M bimetallic Fe-Ag NPs can supply up to 2931 mA h g⁻¹ discharging capacity, corresponding to 10.94 wt% hydrogen storage capacity, which is by far the highest value amongst reported CNT electrodes. It is notable that after 20 cycles, the capacity increased by 379%, with excellent cycling stability, which is highly promising for applications in secondary hydrogen batteries. The demonstrated hydrogen storage capacity is both large and affordable due to the low cost of the primary

materials and the methods involved in this process. As a result, the electrochemical process of adsorption/desorption of hydrogen in carbon materials decorated with transition metals in bimetallic form and transition metal oxides as catalysts is recommended as a hydrogen storage method for the future.

Conflicts of interest

There are no conflicts to declare.

Acknowledgements

This study is based upon work supported partially by the Research Council of Yasouj University, the Protection of Researchers and Technology under grant number 96005467, the National Science Foundation under grant numbers ECCS-1351533, and CMMI-1363485 and AFOSR under contract number FA9550-12-1-0225.

References

- 1 Z. Wang, Z. Shi and Z. Gu, Carbon, 2010, 48, 443-446.
- 2 Z. M. Ao and F. M. Peeters, *Phys. Rev. B: Condens. Matter Mater. Phys.*, 2010, **81**, 205406.
- 3 E. L. Gonzalez, F. I. Llerena, M. S. Perez, F. R. Iglesias and J. G. Macho, *Int. J. Hydrogen Energy*, 2015, **40**, 5518–5525.
- 4 Y. Wu, X. Jiang, J. Chen, Y. Qi, Y. Zhang, H. Fu, J. Zheng and X. Li, *Dalton Trans.*, 2017, **46**, 4499–4503.
- 5 N. N. Sulaiman and M. Ismail, *Dalton Trans.*, 2016, 45, 19380–19388.
- 6 L. Z. Ouyang, W. Chen, J. W. Liu, M. Felderhoff, H. Wang and M. Zhu, Adv. Energy Mater., 2017, 1700299.
- 7 W. Chen, L. Z. Ouyang, J. W. Liu, X. D. Yao, H. Wang, Z. W. Liu and M. Zhu, J. Power Sources, 2017, 359, 400–407.
- 8 H. Zhong, L. Z. Ouyang, J. S. Ye, J. W. Liu, H. Wang, X. D. Yao and M. Zhu, *Energy Storage Mater.*, 2017, 7, 222–228.
- 9 L. Han, W. Qin, J. Jian, J. Liu, X. Wu, P. Gao, B. Hultman and G. Wu, *J. Power Sources*, 2017, 358, 93–100.
- 10 L. Z. Ouyang, Z. J. Cao, H. Wang, R. Hu and M. Zhu, J. Alloys Compd., 2017, 691, 422–435.

- 11 C. Lin, L. Yang, L. Z. Ouyang, J. W. Liu, H. Wang and M. Zhu, J. Alloys Compd., 2017, 728, 578-584.
- 12 L. Z. Ouyang, Z. J. Cao, L. L. Li, H. Wang, J. W. Liu, D. Min, Y. W. Chen, F. M. Xiao, R. H. Tang and M. Zhu, Int. J. Hydrogen Energy, 2014, 39, 12765–12772.
- 13 R. Naresh Muthu, S. Rajashabala and R. Kannan, *Renewable Energy*, 2016, **85**, 387–394.
- 14 H. Nishihara and T. Kyotani, *Adv. Mater.*, 2012, **24**, 4473–4498.
- 15 R. Akbarzadeh and H. Dehghani, *J. Solid State Electrochem.*, 2018, 22, 395–405.
- 16 L. Zhou, X. Qu, D. Zheng, H. Tang, D. Liu, D. Qu, Z. Xie, J. Li and D. Qu, ACS Appl. Mater. Interfaces, 2017, 47, 41332.
- 17 S. W. Hwang, S. U. Rather, M. U. D. Naik, C. S. Soo and K. S. Nahm, *J. Alloys Compd.*, 2009, **480**, 20–24.
- 18 L. Han, W. Qin, J. Zhou, J. Jian, S. Lu, X. Wu, G. Fan, P. Gao and B. Liu, *Nanoscale*, 2017, **9**, 5141–51447.
- 19 A. Lueking and R. T. Yang, J. Catal., 2002, 206, 165-168.
- 20 C. H. Chen and C. C. Huang, *Microporous Mesoporous Mater.*, 2008, **109**, 549–559.
- 21 K.-Yu Lin, W.-Ta Tsai and T.-J. Yang, *J. Power Sources*, 2011, **196**, 3389–3394.
- 22 S. Eugenio, U. B. Demirci, T. M. Silva, M. J. Carmezim and M. F. Montemor, *Int. J. Hydrogen Energy*, 2016, 41, 8438– 8448.
- 23 F. Yang, Y. Zhang, P. F. Liu, Y. Cui, X. R. Ge and Q. S. Jing, Int. J. Hydrogen Energy, 2016, 41, 6773–6780.
- 24 K. Hassan, A. S. M. Iftekhar Uddin and G. S. Chung, Int. J. Hydrogen Energy, 2016, 41, 10991–11001.
- 25 K. Kim and J. I. Han, Int. J. Hydrogen Energy, 2015, 40, 4567–4572.
- 26 K. More, C. Yu, Z. Liu, S. Kaya, D. Nordlund and H. Ogasawara, *Nat. Chem.*, 2010, 2, 454–460.
- 27 Y. Guo and G. Lu, Int. J. Hydrogen Energy, 2016, 41, 6706-6712.
- 28 S. K. Singh, A. K. Singh, K. Aranishi and Q. Xu, *J. Am. Chem. Soc.*, 2011, **133**, 19638–19641.
- 29 S. Chen, B. D. Adams and A. Chen, *Electrochim. Acta*, 2010, **56**, 61–67.
- 30 Y. Lu, R. Jin and W. Chen, Nanoscale, 2011, 3, 2476-2480.
- 31 H. Li, H. Y. Xu and W. Z. Li, J. Membr. Sci., 2008, 324, 44.
- 32 K. Santhi, T. A. Revathy, V. Narayanan and A. Stephen, *Appl. Surf. Sci.*, 2014, **316**, 491–496.
- 33 S. Liu, L. Yin, Y. Koltypin, A. Gedanken, X. Xu, Y. Yeshuru, I. Felner and G. Gorodetsky, *J. Magn. Magn. Mater.*, 2001, 233, 195–204.
- 34 J. M. Abdul and L. H. Chown, *Int. J. Hydrogen Energy*, 2016, **41**, 2781–2787.
- 35 J. H. Yoo, G. Shim, S. W. Cho and C. N. Park, Int. J. Hydrogen Energy, 2007, 32, 2977–2981.
- 36 L. X. Chen, Y. F. Zhu, C. C. Yang, Z. W. Chen, D. M. Zhang and Q. Jiang, *J. Power Sources*, 2016, 333, 17–23.
- 37 D. Heon Lee, M. Kang, S. M. Paek and H. Jung, *Electrochim. Acta*, 2016, 217, 132–138.

- 38 T. K. Nielsen, K. Manickam, M. Hirscher, F. Besenbacher and T. R. Jensen, ACS Nano, 2009, 3, 3521–3528.
- 39 X. H. Tan, C. T. Harrower, B. S. Amirkhiz and D. Mitlin, Int. J. Hydrogen Energy, 2009, 34, 7741–7748.
- 40 H. Barlag, L. Opara and H. Zuchner, *J. Alloys Compd.*, 2002, 330, 434–437.
- 41 Z. Zhang, Z. Zhou, S. Nie, H. Wang, H. Peng, G. Li and K. Chen, *I. Power Sources*, 2014, 267, 388–393.
- 42 Z. Hong, M. Wei, T. Lan and G. Cao, *Nano Energy*, 2012, 1, 466–471.
- 43 X. W. Lou and L. A. Archer, Adv. Mater., 2008, 20, 1583.
- 44 S. T. Myung, N. Takahashi, S. Komaba, C. S. Yoon, Y. K. Sun, K. Amine and H. Yashiro, *Adv. Funct. Mater.*, 2011, 21, 3231–3241.
- 45 Y. Peng, Z. Le, M. Wen, D. Zhang, Z. Chen, H. B. Wu, H. Li and Y. Lu, *Nano Energy*, 2017, 35, 44–51.
- 46 B. Qiu, M. Xing and J. Zhang, J. Am. Chem. Soc., 2014, 136, 5852–5855.
- 47 Z. Chen, Y. Yuan, H. Zhou, X. Wang, Z. Gan, F. Wang and Y. Lu, *Adv. Mater.*, 2014, **26**, 339–345.
- 48 E. Liu, J. Wang, J. Li, C. Shi, C. He, X. Du and N. Zhao, *Int. J. Hydrogen Energy*, 2011, **36**, 6739–6743.
- 49 S. Rather, N. Mehraj-ud-din, R. Zacharia, S. W. Hwang, A. R. Kim and K. S. Nahm, *Int. J. Hydrogen Energy*, 2009, **34**, 961–966.
- 50 S. Liu, R. Yuan, Y. Chai and H. Su, *Sens. Actuators, B*, 2011, **156**, 388–394.
- 51 Y. Wu, J. Zhang, L. Xiao and F. Chen, *Appl. Surf. Sci.*, 2010, **256**, 4260–4268.
- 52 M. S. Dresselhaus, G. Dresselhaus, R. Saito and A. Jorio, *Phys. Rep.*, 2005, **409**, 47–99.
- 53 A. Reyhani, S. Z. Mortazavi, A. Z. Moshfegh, A. Nozad Golikand and M. Amiri, *J. Power Sources*, 2009, **188**, 404–410.
- 54 M. Kaur and K. Pal, *Int. J. Hydrogen Energy*, 2016, **41**, 21861–21869.
- 55 M. Latroche, J. Phys. Chem. Solids, 2004, 65, 517-522.
- 56 Ch. Chang, P. Gao, D. Bao, L. Wang, Y. Wang, Y. Chen, X. Zhou, Sh. Sun, G. Li and P. Yang, *J. Power Sources*, 2014, 255, 318–324.
- 57 S. Li, W. Pan and Z. Mao, *Int. J. Hydrogen Energy*, 2005, **30**, 643–648.
- 58 X. Chen, X. P. Gao, H. Zhang, Z. Zhou, W. K. Hu and G. L. Pan, *J. Phys. Chem. B*, 2005, **109**, 11525–11529.
- 59 R. Akbarzadeh, M. Ghaedi, S. Nasiri Kokhdan, R. Jannesar, F. Sadeghfar, F. Sadri and L. Tayebi, *Int. J. Hydrogen Energy*, 2018, 43, 18316–18329.
- 60 C. C. Yang, Y. J. Li and W. H. Chen, *Int. J. Hydrogen Energy*, 2010, 35, 2336–2343.
- 61 S. C. Mu, H. L. Tang, S. H. Qian, M. Pan and R. Z. Yuan, *Carbon*, 2006, **44**, 762–767.
- 62 R. Jianwei, L. Shijun and L. Junmin, *Chin. Sci. Bull.*, 2006, **51**, 2959–2963.
- 63 H. Zhang, X. Fu, J. Yin, C. Zhou, Y. Chen, M. Li and A. Wei, *Phys. Lett. A*, 2005, **339**, 370–377.